An Analytic Solution for the Noise Generated by Gust-Aerofoil Interaction for Plates with Serrated Leading Edges

LORNA J. AYTON †[1] and JAE WOOK KIM [2]

[1]Department of Applied Mathematics and Theoretical Physics, University of Cambridge, Wilberforce Road, CB3 0WA, UK
[2]Aerodynamics & Flight Mechanics Research Group, University Road, University of Southampton, Southampton, SO17 1BJ, UK

(Received 23 July 2018)

This paper presents an analytic solution for the sound generated by an unsteady gust interacting with a semi-infinite flat plate with a serrated leading edge in a background steady uniform flow. Viscous and non-linear effects are neglected. The Wiener-Hopf method is used in conjunction with a non-orthogonal coordinate transformation and separation of variables to permit analytical progress. The solution is obtained in terms of a modal expansion in the spanwise coordinate, however for low- and mid-range incident frequencies only the zeroth order mode is seen to contribute to the far-field acoustics, therefore the far-field noise can be quickly evaluated. The solution gives insight into the potential mechanisms behind the reduction of noise for plates with serrated leading edges compared to those with straight edges, and predicts a logarithmic dependence between the tip-to-root serration height and the decrease of far-field noise. The two mechanisms behind the noise reduction are proposed to be an increased destructive interference in the far field, and a redistribution of acoustic energy from low cuton modes to higher cutoff modes as the tip-to-root serration height is increased. The analytic results show good agreement in comparison with experimental measurements. The results are also compared against non-linear numerical predictions where good agreement is also seen between the two results as frequency and tip-to-root ratio are varied.

1. Introduction

Leading-edge noise is generated by the unsteady wakes of a forward rotor row impinging on a rearward stator row within an aeroengine. It is well known as a dominant source of aircraft noise (Peake & Parry 2012) and as such has sparked a large amount of research aimed at understanding and controlling noise levels (Amiet 1975; Goldstein & Atassi 1976; Myers & Kerschen 1995; Lockard & Morris 1998; Ayton & Chaitanya 2017). Recent interest in silent owl flight has led to research in a number of aerofoil adaptations as a way to reduce aerofoil-turbulence interaction noise as discussed by Lilley (1998). The leading-edge comb (Graham 1934) appears as a serration to the leading edge of the wing, and through experimental (Geyer *et al.* 2016; Chaitanya *et al.* 2016) and numerical investigations (Haeri *et al.* 2015; Kim *et al.* 2016) has been seen as an effective way to reduce leading-edge noise. Despite these results, it is still not fully understood why the serrated edge is such an effective way to reduce leading-edge noise, therefore analytic

† Email address for correspondence: L.J.Ayton@damtp.cam.ac.uk

solutions for simple leading-edge interaction noise models are sought to illuminate the physical noise-reduction mechanisms within the flow, and hence aid in designing optimal leading-edge geometries for silent blade operation.

Current analytic models for leading-edge serrations such as the gust-interaction noise model of Lyu & Azarpeyvand (2017) or the sound scattering model of Huang (2017) typically rely on standard Fourier series expansions in the spanwise coordinate (along which the serration lies) and iterative or numerical techniques to eventually solve the final governing equations. A downside of this is that it becomes difficult to extract precise information from the solutions as to why a reduction of noise is possible, as one cannot pick apart the final solution to determine when and where each term has come from. Solutions from the iterative method using the Schwartzchild technique (Lyu & Azarpeyvand 2017) predict that the noise reduction for rapidly serrated edges may differ from those predicted experimentally (Chaitanya *et al.* 2016) since it is typical that experimentally noise is measured in a restricted arc centred above the plate. This misses the far upstream and downstream directions; the solution (Lyu & Azarpeyvand 2017) predicts that the acoustic directivity pattern is significantly distorted by rapid serrations, which could result in larger or smaller pressure magnitudes at shallow angles than the effects seen directly above the plate (at $\theta = 90°$).

Both Lyu & Azarpeyvand (2017)'s analytical and Chaitanya *et al.* (2016)'s experimental results suggest that phase interference in the scattered field are key to noise reduction for rapidly serrated edges, and a greater noise reduction is possible for more rapidly serrated edges due to an increased destructive interference. However if the far field were to experience a region of destructive interference it would be natural to assume there could be a corresponding region of constructive interference. The analytic solution obtained via Green's functions for the sound generated by individual vortices interacting with a wavy leading edge by Mathews & Peake (2018) indicates certain leading-edge profiles do increase noise as opposed to reducing it. Key to an increase or decrease in noise is the relative angle between the vortex path and the leading edge, which is also an important factor for swept leading edges (Adamczyk 1974). Huang (2017) who uses a Wiener-Hopf approach proposes a reduction of far-field noise due to a cutoff of the scattered frequency, as is the case for the swept edge (Adamczyk 1974), however similarly to Lyu & Azarpeyvand (2017), it is difficult to infer this conclusion directly from the mathematics as the details are unfortunately hidden by the complexity surrounding the Fourier series expansions and numerical Wiener-Hopf factorisation.

This paper attempts to provide a simpler analytic solution for the noise generated by a serrated leading edge, which can be used to understand the mechanisms allowing for noise reduction. We avoid the need for any numerical steps during the calculation of the far-field pressure by using a sequence of variable transformations to convert the governing equation and boundary conditions into a form suitable for solving analytically using the Wiener-Hopf technique. We also avoid the need for numerically factorising the Wiener-Hopf kernel. This approach follows the work of Envia (1988) who considered the effects of blade sweep in a finite-span channel with rigid walls.

The layout of this paper is as follows. The governing equation and boundary conditions for the problem are given in Section 2 along with the required transformation of coordinates to allow for a simple solution. The solution is found in Section 3 using separation of variables and the Wiener-Hopf technique. Section 4 contains results for the scattered acoustic far field which we compare to numerical simulations adapted from Turner & Kim (2017). A brief discussion of the adapted numerical method used is given in Section 4.5. We discuss the conclusions of this paper in Section 5.

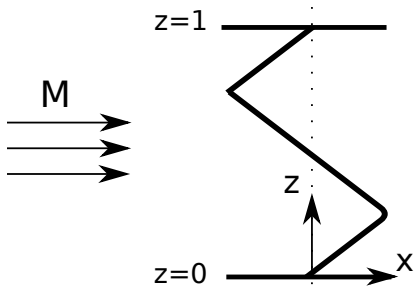

Figure 1: Uniform steady flow in the x direction with unsteady convective gust perturbation interacts with a rigid plate $y = 0$ with serrated edge $x = cF(z)$.

2. Formulation of the Problem

We consider the interaction of a convective unsteady gust in uniform flow of Mach number M over a semi-infinite flat plate with a serrated leading edge. To simplify the problem we consider a single wavelength of the serration, thus the blade lies in the region $y = 0$, $x > cF(z)$, $0 \leqslant z \leqslant 1$ as depicted in Figure 1. Here c is a positive real constant parameterising the so-called 'tip-to-root' height of the serration (which is given by $c/2$). We non-dimensionalise lengths by the wavelength of the serration, and velocities by the far upstream steady velocity. Pressure is non-dimensionalised with respect to the far upstream steady density and velocity.

We suppose the serration is single-frequency, therefore define

$$F(z) = \begin{cases} z, & z \in [0, \frac{1}{4}) \\ \frac{1}{2} - z, & z \in (\frac{1}{4}, \frac{3}{4}) \\ z - 1, & z \in (\frac{3}{4}, 1] \end{cases} \tag{2.1}$$

Note the channel boundaries are located at serration midpoints to ensure any effects of the sharp tip and root at $z = 1/4, 3/4$ are fully accounted for and the edges do not interfere with these key features.

The unsteady gust incident from far upstream takes the form

$$\boldsymbol{v}_g = \boldsymbol{A} \mathrm{e}^{ik_1 x + ik_2 y + ik_3 z - i\omega t}, \tag{2.2}$$

where the amplitude, $\boldsymbol{A} = (A_1, A_2, A_3)^T$, is constant.

We consider two cases for the scattered field: a) the channel has rigid walls thus there is a single wavelength serrated blade in a duct; and b) the channel has periodic boundary conditions. In both cases we set $A_3 = 0$, and as we are dealing with an infinitely thin plate the only amplitude term from the gust present in our problem will be A_2, which for simplicity we set to unity. Case a) allows us to compare the effects of a serrated edge against that of a swept edge in a channel (Envia 1988), whilst case b) allows us to consider a spanwise-infinite plate with a periodic serrated leading edge.

We decompose the unsteady flow field into a convective gust part and an acoustic response part, $\boldsymbol{v} = \boldsymbol{v}_g + \boldsymbol{v}_a$, and write the response as $\boldsymbol{v}_a = \nabla G$. We suppose G is harmonic in time $\sim \mathrm{e}^{-i\omega t}$ therefore spatially satisfies the convected Helmholtz equation,

$$\beta^2 \frac{\partial^2 G}{\partial x^2} + \frac{\partial^2 G}{\partial y^2} + \frac{\partial^2 G}{\partial z^2} + 2ikM \frac{\partial G}{\partial x} + k^2 G = 0, \tag{2.3}$$

where $\beta^2 = 1 - M^2$ and $k = \omega / c_0$ with c_0 the speed of sound of the background steady flow. Since the gust convects with the background flow, we require $k = k_1 M$. The zero

normal velocity boundary condition on the aerofoil surface requires

$$\left.\frac{\partial G}{\partial y}\right|_{y=0} = -\mathrm{e}^{ik_1 x + ik_3 z} \qquad x > cF(z). \tag{2.4a}$$

We also impose continuity of the potential upstream

$$\Delta G|_{y=0} = 0 \qquad x < cF(z). \tag{2.4b}$$

Finally, in case a) the rigid channel walls require

$$\left.\frac{\partial G}{\partial z}\right|_{z=0,1} = 0, \tag{2.5a}$$

or case b) the periodic conditions yield

$$G|_{z=0} = G|_{z=1}\mathrm{e}^{i\alpha k_3}, \qquad \left.\frac{\partial G}{\partial z}\right|_{z=0} = \left.\frac{\partial G}{\partial z}\right|_{z=1} \mathrm{e}^{i\alpha k_3}, \tag{2.5b}$$

where α is a real constant enforcing the level of periodicity of the problem, e.g. if $\alpha = -1$ the solution must be periodic over one serration wavelength or if $\alpha = -1/2$ the solution must be periodic over two serration wavelengths. We will restrict results in this paper to $\alpha = -1$ however retain the parameter in our calculations to allow a future study on varying the periodicity of the solution.

To simplify the governing equation, (2.3), we apply a convective transform,

$$h = G(x, y, z)\mathrm{e}^{ik_1 M^2 x/\beta^2}, \tag{2.6}$$

to eliminate the convective terms. The resulting governing equation and boundary conditions for $h(x, y, z)$ are

$$\beta^2 \frac{\partial^2 h}{\partial x^2} + \frac{\partial^2 h}{\partial y^2} + \frac{\partial^2 h}{\partial z^2} + \left(\frac{k_1 M}{\beta}\right)^2 h = 0, \tag{2.7a}$$

$$\left.\frac{\partial h}{\partial y}\right|_{y=0} = -\mathrm{e}^{i\frac{k_1}{\beta^2}x + ik_3 z} \qquad x > cF(z), \tag{2.7b}$$

$$\Delta h|_{y=0} = 0 \qquad x < cF(z), \tag{2.7c}$$

accompanied by the option of a rigid vertical wall condition (case a) or periodic condition (case b) on $z = 0, 1$ as before.

This set of equations, (2.7), forms a mixed boundary condition problem in regions $x \gtrless cF(z)$ therefore we wish to employ the Wiener-Hopf technique. However to make this problem more amenable to the Wiener-Hopf technique we wish to shift the two regions to some $\xi \gtrless 0$ making them independent of the spanwise variable. To do so we perform the following transformation of coordinates (adapted from the transformation used by Envia (1988) for a swept edge);

$$\xi = \frac{\sqrt{1-\gamma^2}}{\beta} x - \gamma F(z), \tag{2.8a}$$

$$\eta = y, \tag{2.8b}$$

$$\zeta = z, \tag{2.8c}$$

$$\gamma = \frac{c}{\sqrt{\beta^2 + c^2}}. \tag{2.8d}$$

The transformed governing equation becomes

$$\nabla^2_{\xi,\eta,\zeta} h - 2\gamma F'(\zeta)\frac{\partial^2 h}{\partial \xi \partial \zeta} + (dM)^2 h = \gamma\left(\delta(\zeta - \frac{3}{4}) - \delta(\zeta - \frac{1}{4})\right)\frac{\partial h}{\partial \xi}, \tag{2.9a}$$

where we set $d = k_1/\beta$ and use $\delta(x)$ to denote the Dirac delta function arising due to the discontinuities in $F'(\zeta)$ at the peaks and roots of the serration. Note the right hand side equals $\gamma F''(\zeta)\frac{\partial h}{\partial \xi}$, and derivatives of F are formally weak derivatives.

The boundary conditions become

$$\left.\frac{\partial h}{\partial \eta}\right|_{\eta=0} = -\mathrm{e}^{i\kappa\xi + ik_3\zeta}\mathrm{e}^{i\kappa\gamma F(\zeta)} \quad \xi > 0, \tag{2.9b}$$

where $\kappa = d/\sqrt{1-\gamma^2}$,

$$\Delta h|_{\eta=0} = 0 \quad \xi < 0, \tag{2.9c}$$

and either for the rigid walls of case a);

$$\left(\frac{\partial h}{\partial \zeta} - \gamma F'(\zeta)\frac{\partial h}{\partial \xi}\right)_{\zeta=0,1} = 0, \tag{2.9d}$$

or for the periodic conditions of case b);

$$G|_{\zeta=0} = G|_{\zeta=1}\mathrm{e}^{i\alpha k_3}, \qquad \left.\frac{\partial G}{\partial \zeta}\right|_{\zeta=0} = \left.\frac{\partial G}{\partial \zeta}\right|_{\zeta=1}\mathrm{e}^{i\alpha k_3}. \tag{2.9e}$$

We have now completed the formulation of the mathematical model, which we shall solve in the following section.

3. Analytic Solution

We solve (2.9) by applying a Fourier transform in the ξ variable,

$$H(\lambda,\eta,\zeta) = \int_{-\infty}^{\infty} h(\xi,\eta,\zeta)\mathrm{e}^{i\lambda\xi}d\xi, \tag{3.1}$$

and separating the solution $H(\lambda,\eta,\zeta) = Y(\lambda,\eta)Z(\lambda,\zeta)$ with separation constant $\tilde{\chi}$. This results in governing equations

$$Y'' + \left((dM)^2 - \lambda^2 - \tilde{\chi}^2\right)Y = 0, \tag{3.2}$$

and

$$Z'' + 2i\gamma\lambda F'(\zeta)Z' + \tilde{\chi}^2 Z = -i\lambda\gamma\left(\delta(\zeta - \frac{3}{4}) - \delta(\zeta - \frac{1}{4})\right)Z, \tag{3.3}$$

for the η and ζ dependencies.

We solve (3.3) by considering an ansatz of the form

$$Z(\lambda,\zeta) = \mathrm{e}^{-i\gamma\lambda F(\zeta)}\left(A(\lambda)\cos(\chi\zeta) + B(\lambda)\sin(\chi\zeta)\right), \tag{3.4}$$

which is found to satisfy (3.3) when $\chi^2 = \lambda^2\gamma^2 + \tilde{\chi}^2$. This yields solutions for Y given by

$$Y(\lambda,\eta) = \mathrm{sgn}(\eta)\mathrm{e}^{-|\eta|\sqrt{1-\gamma^2}\sqrt{\lambda^2 - w^2}}, \tag{3.5}$$

where

$$w^2 = \frac{(dM)^2 - \chi^2}{1-\gamma^2}. \tag{3.6}$$

To determine suitable values for χ and a relationship between $A(\lambda)$ and $B(\lambda)$ we must apply the boundary conditions to Z at $\zeta = 0, 1$. These give rise to a modal expansion of the solution indexed by n. Using the rigid walled condition, (2.9d), yields

$$Z(\lambda,\zeta) = A_n(\lambda)Z_n(\lambda,\zeta) = \mathrm{e}^{-i\gamma\lambda F(\zeta)}A_n(\lambda)\cos(n\pi\zeta), \quad \chi = n\pi, \quad n \in \mathbb{Z}, \tag{3.7}$$

whilst the periodic condition, (2.9e), yields

$$Z(\lambda,\zeta) = A_n(\lambda)Z_n(\lambda,\zeta) = \mathrm{e}^{-i\gamma\lambda F(\zeta)}A_n(\lambda)\mathrm{e}^{-ik_3\alpha\zeta}\mathrm{e}^{2in\pi\zeta}, \quad \chi = \pm k_3\alpha + 2n\pi, \quad n \in \mathbb{Z}. \tag{3.8}$$

We must now determine the $A_n(\lambda)$ using the $\eta = 0$ boundary conditions and the Wiener-Hopf method. We can write the general solution as

$$H(\lambda,\eta,\zeta) = \sum_n A_n(\lambda)\mathrm{sgn}(\eta)\mathrm{e}^{-|\eta|\sqrt{1-\gamma^2}\sqrt{\lambda^2-w_n^2}}Z_n(\lambda,\zeta), \tag{3.9}$$

where the Z_n are either given in (3.7) or (3.8). The upstream continuity condition, (2.9c), tells us $A_n(\lambda)$ is a positive half-Fourier transform only, therefore is analytic in the upper half $\lambda-$plane which we denote by a superscript $+$ (analyticity in the lower half plane is similarly denoted by a superscript $-$).

The zero normal velocity condition, (2.9b), upon applying the Fourier transform becomes

$$\frac{\partial H}{\partial \eta}(\lambda,0,\zeta) = K^+(\lambda,\zeta) + U^-(\lambda,\zeta) \tag{3.10}$$

where

$$K^+(\lambda,\zeta) = -\frac{i}{\lambda+\kappa}\mathrm{e}^{i\kappa\gamma F(\zeta)+ik_3\zeta} \tag{3.11}$$

and $U^-(\lambda,\zeta)$ is an unknown function which is analytic in the lower half $\lambda-$plane. Using (3.9) we obtain

$$-\sum_n \sqrt{1-\gamma^2}\sqrt{\lambda^2-w_n^2}A_n^+(\lambda)Z_n(\lambda,\zeta) = -\frac{i}{\lambda+\kappa}\mathrm{e}^{i\kappa\gamma F(\zeta)+ik_3\zeta} + U^-(\lambda,\zeta). \tag{3.12}$$

The functions $Z_n(\lambda,\zeta)$ are orthogonal over the range $\zeta \in [0,1]$ with respect to their Schwartz conjugates thus we can use them as a basis for expanding our known and unknown functions. In particular $U^-(\lambda,\zeta)$ can be expressed as

$$U^-(\lambda,\zeta) = \sum_n D_n(\lambda)Z_n(\lambda,\zeta) \tag{3.13}$$

and we write $\mathrm{e}^{i\kappa\gamma F(\zeta)+ik_3\zeta}$ as

$$\mathrm{e}^{i\kappa\gamma F(\zeta)+ik_3\zeta} = \sum_n E_n(\lambda)Z_n(\lambda,\zeta). \tag{3.14}$$

The functions $E_n(\lambda)$ arise because of the spanwise form of the normal velocity on the plate and are given in the Appendix A. If we suppose, like Envia (1988), that the normal velocity just upstream of the plate must have a similar spanwise ζ dependence, then by linearity each A_n^+ and each D_n^- must contain a factor of $E_n(\lambda)$ †.

We factor out E_n in our Wiener-Hopf equation to obtain

† To assume this we must also neglect any boundary layer effects due to the channel walls at $\zeta = 0, 1$. We believe this is a suitable assumption as we are interested not in the effects of the channel walls, but solely in the effects of the serration

$$\sqrt{1-\gamma^2}\sqrt{\lambda^2-w_n^2}\tilde{A}_n^+(\lambda) = \frac{i}{\lambda+\kappa} + \tilde{D}_n(\lambda), \tag{3.15}$$

where

$$\tilde{A}_n^+ E_n = A_n^+, \qquad \tilde{D}_n^- E_n = D_n^- \tag{3.16}$$

The $E_n(\lambda)$ are entire, therefore we can factor them out of the terms A_n^+ and D_n^- without affecting the domain of analyticity.

We rearrange (3.15) to give

$$\sqrt{1-\gamma^2}\sqrt{\lambda+w_n}\tilde{A}_n^+(\lambda) = \frac{i}{\lambda+\kappa}\frac{1}{\sqrt{\lambda-w_n}} - \frac{D_n^-(\lambda)}{\sqrt{\lambda-w_n}}. \tag{3.17}$$

The left hand side is analytic in the upper half $\lambda-$plane, and the unknown term on the right hand side is analytic in the lower half $\lambda-$plane. By additively splitting the known term on the right hand side into two functions, $F_n^+ + F_n^-$, that are analytic in the appropriate half planes we can apply Liouville's theorem to solve for $\tilde{A}_n^+(\lambda)$ giving

$$\tilde{A}_n^+(\lambda) = \frac{F_n^+(\lambda)}{\sqrt{1-\gamma^2}\sqrt{\lambda+w_n}}, \tag{3.18}$$

with

$$F_n^+(\lambda) = \frac{i}{\lambda+\kappa}\frac{1}{\sqrt{-\kappa-w_n}}, \tag{3.19}$$

hence

$$H(\lambda,\eta,\zeta) = \mathrm{sgn}(\eta)\sum_n \frac{F_n^+(\lambda)E_n(\lambda)\mathrm{e}^{-|\eta|\sqrt{1-\gamma^2}\sqrt{\lambda^2-w_n^2}}}{\sqrt{1-\gamma^2}\sqrt{\lambda+w_n}} Z_n(\lambda,\zeta). \tag{3.20}$$

We invert the Fourier transform and obtain the far-field ($r \gg 1$) acoustics by applying the method of steepest descents to give

$$h(r,\theta,z) \sim$$
$$\sum_n \frac{\mathrm{e}^{\pi i/4}F_n^+(-w_n\cos\theta)E_n(-w_n\cos\theta)}{(1-\gamma^2)^{3/4}\sqrt{\pi}}\cos\left(\frac{\theta}{2}\right)\frac{\mathrm{e}^{i\sqrt{1-\gamma^2}w_n r}}{\sqrt{r}}Z_n(-w_n\cos\theta,z)\mathrm{e}^{-i\gamma w_n\cos\theta F(z)}, \tag{3.21}$$

where (r,θ,z) are standard cylindrical polar coordinates with origin corresponding to Cartesian origin $x=y=z=0$. For simplicity, we write (3.21) as

$$h(r,\theta,z) \sim \sum_n B_n(\theta,z)\frac{\mathrm{e}^{i\sqrt{1-\gamma^2}w_n r}}{\sqrt{r}}, \tag{3.22}$$

where we refer to the B_n as the scattered modes with frequencies $\sqrt{1-\gamma^2}w_n$. We recall the definition of w_n in (3.6) and see that for sufficiently large n these modes are cutoff, therefore practically we only need to sum a finite number of terms in (3.22) to calculate this far-field expression.

To obtain the acoustic pressure, we use the relation

$$p = -\left(\frac{\partial h}{\partial x} - \frac{ik_1}{\beta^2}h\right)\mathrm{e}^{-ik_1M^2x/\beta^2}, \tag{3.23}$$

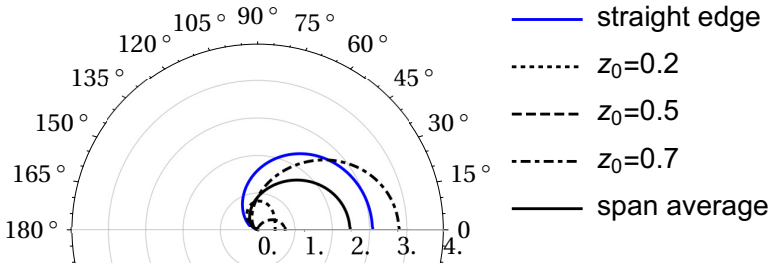

Figure 2: Polar plot of $10^3|p(10,\theta,z)|^2$ compared to the span average, $10^3 D_a(10,\theta)$, and straight-edge, $c=0$, results, for blades in a rigid walled channel. In all cases $M=0.3$, $k_3=0$, $k_1=10$. Serrated blades have $c=1$.

which in the far field, $r \gg 1$, using (3.22) yields

$$p(r,\theta,z) \sim \sum_n i\left(\frac{k_1}{\beta^2} - \sqrt{1-\gamma^2}w_n\right) B_n(\theta,z)\frac{\mathrm{e}^{i\sqrt{1-\gamma^2}w_n r}}{\sqrt{r}}. \tag{3.24}$$

This completes our analytic solution of the scattered field.

4. Results

In this section we present far-field noise results for both the rigid-walled channel and periodic channel. To do so, we define a spanwise averaged far-field pressure, as

$$D_a(r,\theta) = \int_0^1 |p(r,\theta,z)|^2 dz, \tag{4.1}$$

where $p(r,\theta,z)$ is given by (3.24). We evaluate this numerically, using Mathematica's inbuilt NIntegrate feature. We only sum a finite number of terms from (3.24) corresponding to the cuton terms with $w_n \in \mathbb{R}$. The number of cuton terms depends on the gust wavenumber components, $k_{1,3}$, and the Mach number of the background flow, M. Figure 2 illustrates a variation in $|p(r,\theta,z)|^2$ with spanwise location, z. Different spanwise locations can produce different directivity patterns at different magnitudes due to interference between different B_n modes. We see in Figure 2 that the spanwise averaged pressure recovers the cardiod pattern typically associated with a straight-edge interaction, and we believe the spanwise average gives the best indication of the overall noise generated in the channel.

The layout of this results section is as follows. First in section 4.1 we replicate the results from Envia (1988) for a swept blade in a rigid walled channel and compare to our serrated blade in a channel. Second in section 4.2 we present results for the far-field noise from a serrated edge in a periodic channel, and we discuss how the far-field results are affected by the channel wall conditions, with attention given to noise generated by gusts with both zero and non-zero spanwise wavenumbers, k_3. By noting the importance of the spanwise wavenumber on the far-field sound, in section 4.3 we integrate over a spectrum of k_3 values to compare the far-field power spectral density calculated analytically to that measured experimentally from (Narayanan *et al.* 2015). We use the analytic results to infer noise reduction mechanisms for the serrated leading edge in section 4.4. Finally in section 4.5 we compare the analytic results against numerical predictions.

4.1. *Spanwise averaged far-field pressure in a rigid walled channel*

Here we compare the span averaged directivity for a serrated blade in a channel to a swept blade in a channel (known from Envia (1988)) in Figure 3. We see that the swept blade is more effective at reducing the far-field noise than the serration across all frequency ranges as the gradient of the edges (sweep angle or serration tip-to-root height) increase. To understand this we consider the individual modes contributing to the solutions in each case.

In Figure 4 we plot the amplitude of the modes, $|B_n(\theta, z)|$, from (3.24), contributing to the scattered field for $k_1 = 50$, $c = 1$. We choose a very high frequency as this permits more scattered modes. We clearly see the modes for the swept blade are more oscillatory, thus encounter a greater destructive interference than the modes for the serrated edge. This is to be expected as the greatest horizontal distance between points for the swept blade is twice that of the serrated edge (the swept edge effectively has $F(z) = z$ rather than our definition of (2.1)), and indeed the effective oscillations seen for the swept blade are twice those seen for the serrated edge (compare Figure 5 to Figure 4a). This equivalence between the 0th modes does not occur for higher modes, as these account for more complicated leading-edge geometry effects, and none of the modes are equivalent if $k_3 \neq 0$ as the modal expansions are heavily dependent on k_3 (spanwise variations in the flow expanded in different spanwise bases certainly shouldn't be equivalent). We also note that the oscillations in the modes decreases with increasing mode number; the zeroth mode is the most oscillatory. This is to be expected given that for mid-frequency interactions (such as $k_1 = 5$) only the zeroth mode propagates to the far field yet we see a highly oscillatory directivity for large c. Note, the second mode, B_2, for case a) has a coefficient of zero (as indeed do all $B_{2(2n+1)}$ for $n = 0, 1, \dots$).

4.2. *Spanwise averaged far-field pressure in a periodic channel*

We now consider the spanwise average directivity, $D_a(r, \theta)$, for the periodic case b). In Figure 6 we plot $D_a(r, \theta)$ over the same range of frequency and serration height as Figure 3 when $k_3 = 0$. We see great similarity between the two figures since for low and mid-range frequencies only the 0th order mode propagates to the far field, and these contributions are the same when $k_3 = 0$ (they yield the same E_0 coefficients). For higher frequencies (illustrated by $k_1 = 10$), or when $k_3 \neq 0$ we expect to see different behaviour between case a) and b) as the E_n coefficients contributing to the far-field acoustics are no longer identical.

In Figure 7 we compare cases a) and b) when $k_3 \neq 0$. For the periodic boundary conditions of case b) a non-zero k_3 can cutoff all scattered frequencies w_n, but this is not true in the rigid walled case a). This cutoff is similar to a spanwise-infinite straight edge and is therefore not specifically a feature of the serration. Note when cutoff the results only include the first 6 modes. For the cases that are not cutoff, the periodic serrated edge (case b), shows the ability to increase noise versus a straight edge ($c = 0$) for large k_1 and similar sized k_3 (Figure 7d) when $c \leqslant 1$, however a reduction of noise occurs for $c \geqslant 2$. The walled serration, case a), sees little noise reduction in similar circumstances (Figure 7c), but only exhibits a consistent noise increase with increasing c when k_3 is significantly larger than k_1. We note for high k_1 and (relative) small k_3, such as Figure 7a,7b, the periodic serration results in a slightly greater reduction of far-field noise than the walled serration.

Overall we see serrations either in a rigid walled channel or periodic channel reduce gust interaction noise with increasing serration heights. Some increases of noise can also occur for low tip-to-root heights.

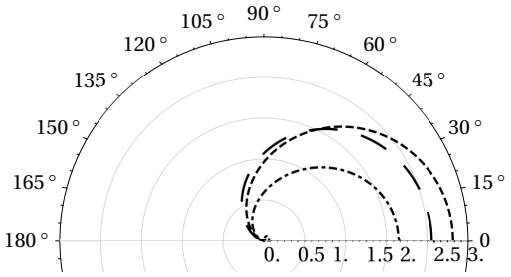

(a) $k_1 = 10$, Case a).

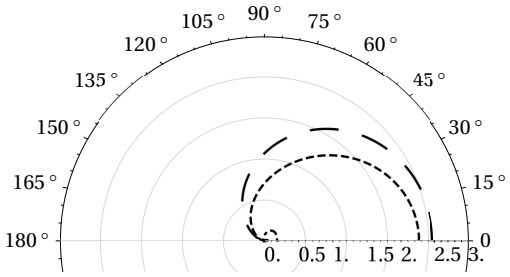

(b) $k_1 = 10$, swept blade.

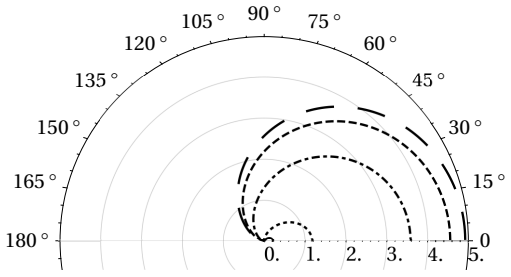

(c) $k_1 = 5$, Case a).

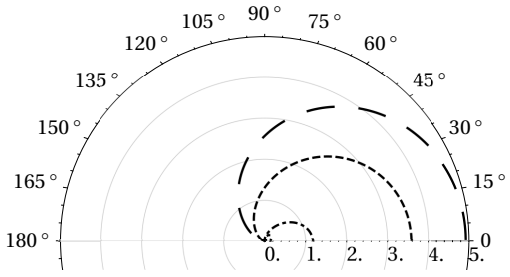

(d) $k_1 = 5$, swept blade.

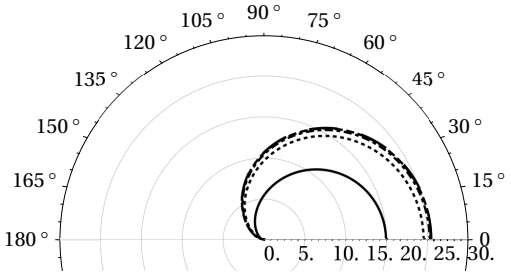

(e) $k_1 = 1$, Case a).

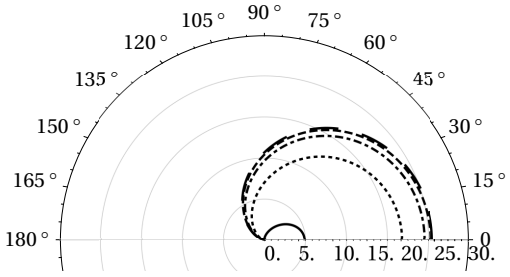

(f) $k_1 = 1$, swept blade.

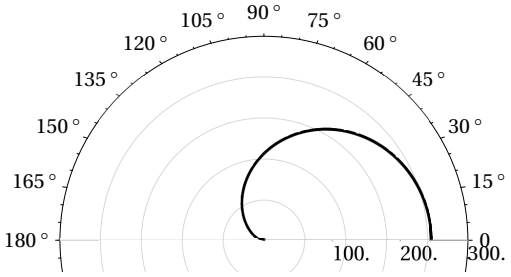

(g) $k_1 = 0.1$, Case a).

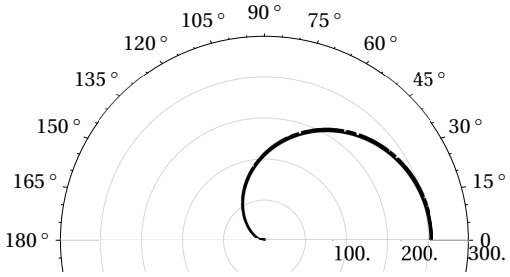

(h) $k_1 = 0.1$, swept blade.

Figure 3: Polar plot of the spanwise average directivity, $10^3 D_a(r, \theta)$ as given by (4.1), for $r = 10$, $M = 0.3$, $k_3 = 0$. Large dashed $c = 0$; dashed $c = 0.5$; dot-dashed $c = 1$; dotted $c = 2$, solid $c = 5$.

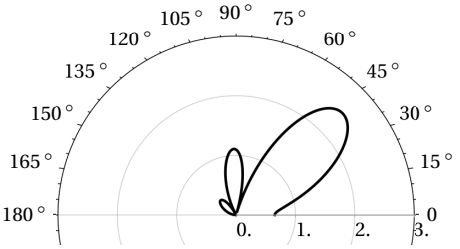

(a) $|B_0(\theta, 0.5)|$, Case a).

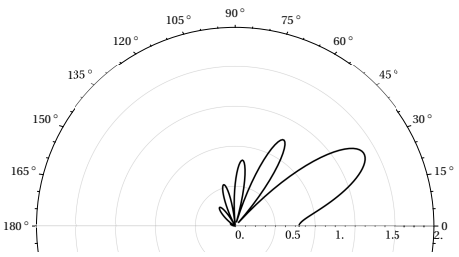

(b) $|B_0(\theta, 0.5)|$, swept blade.

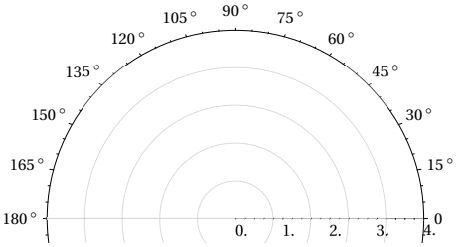

(c) $|B_2(\theta, 0.5)|$, Case a).

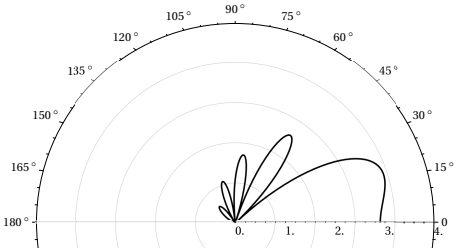

(d) $|B_2(\theta, 0.5)|$, swept blade.

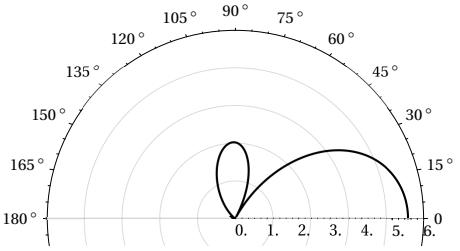

(e) $|B_4(\theta, 0.5)|$, Case a).

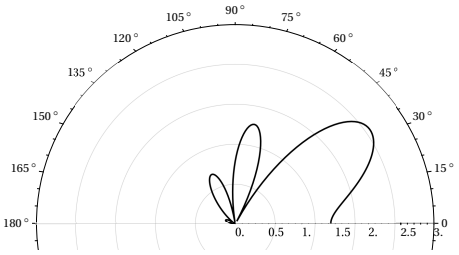

(f) $|B_4(\theta, 0.5)|$, swept blade.

Figure 4: Polar plot of the magnitude of the nth mode, $10^4|B_n(\theta, z)|$, as defined in (3.24), at mid-span point $z = 0.5$, for $M = 0.3$, $k_3 = 0$, $k_1 = 50$.

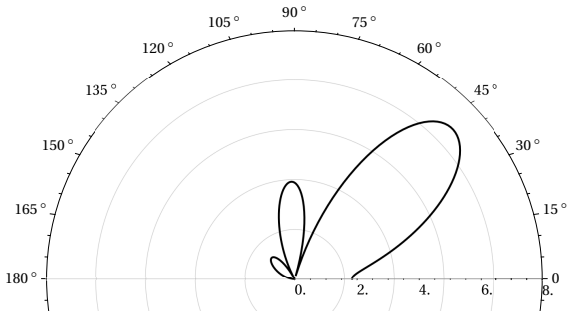

Figure 5: Polar plot of $10^4|B_0(\theta, 0.5)|$ for $M = 0.3$, $k_3 = 0$, $k_1 = 25$ for a swept blade in a rigid channel.

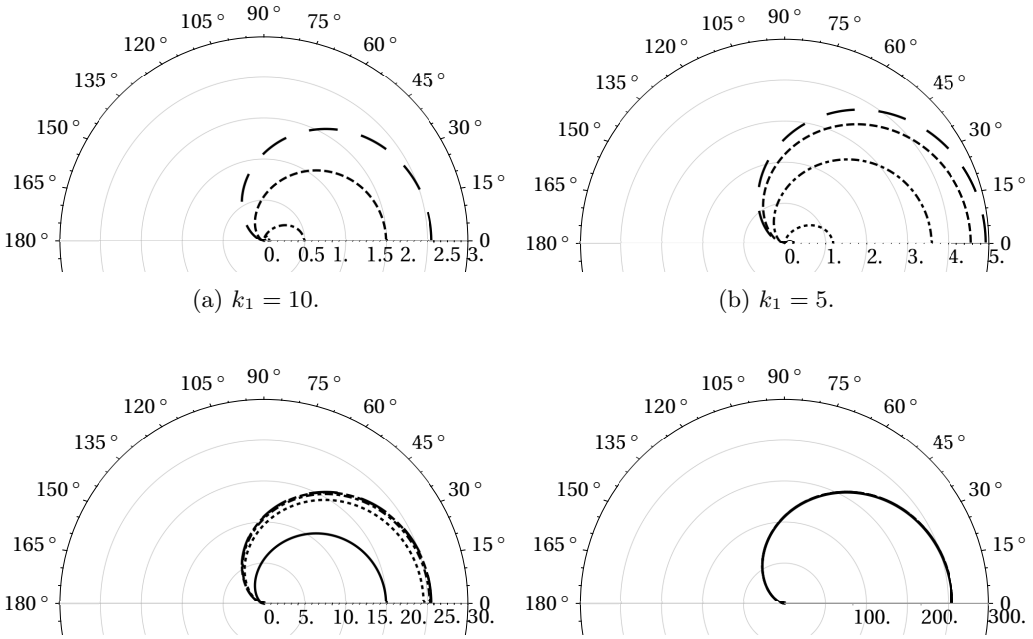

(a) $k_1 = 10.$ (b) $k_1 = 5.$

(c) $k_1 = 1.$ (d) $k_1 = 0.1.$

Figure 6: Polar plot of the spanwise average directivity, $10^3 D_a(r, \theta)$ as given by (4.1), for case b) (periodic channel) with $r = 10$, $M = 0.3$, $k_3 = 0$. Large dashed $c = 0$; dashed $c = 0.5$; dot-dashed $c = 1$; dotted $c = 2$, solid $c = 5$.

4.3. *Far-field PSD for periodic channel*

In the previous sections we have considered the far-field noise at fixed k_3 values. In this section we integrate over a spectrum of k_3 values to calculate the far-field power spectral density (PSD) and compare to experimental measurements from Narayanan *et al.* (2015). We use an upstream spectrum defined by

$$\Phi^{(\infty)}(k_1, k_3) = \frac{k_1^2/k_e^2 + k_3^2/k_e^2}{(1 + k_1^2/k_e^2 + k_3^2/k_e^2)^{7/3}}, \tag{4.2}$$

where

$$k_e = \frac{\sqrt{\pi}\,\Gamma(5/6)}{\Gamma(1/3) L_t},$$

and $L_t = 0.6$ is the non-dimensionalised lengthscale of turbulence. The far-field PSD is thus defined as

$$\text{PSD} = \int_{-\infty}^{\infty} |p(r, \theta, z)|^2 \Phi^{(\infty)}(k_1, k_3) dk_3. \tag{4.3}$$

Large k_3 values have been seen to cut off the scattered field, thus in practice when numerically evaluating this quantity from the analytic expression for p, we integrate only over a finite range of k_3 corresponding to cut on modes.

In Figure 8 we compare the analytic predictions for the PSD to experimental measurements from Narayanan *et al.* (2015), taken at $\theta = \pi/2$, and mid-span $z = 0.5$. The serrations correspond to $c = 2, 4$. We see very good agreement between the analytic and experimental results at mid-range frequencies, indicating that the simple analytic model is capturing all of the key physics behind the noise reductions. We do not expect

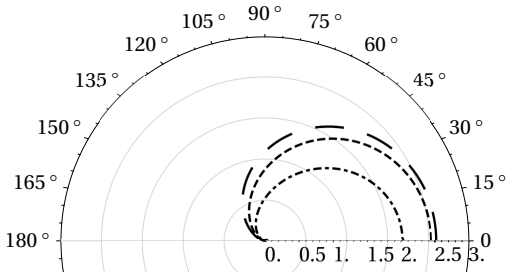

(a) $k_1 = 10$, $k_3 = 1$, Case a).

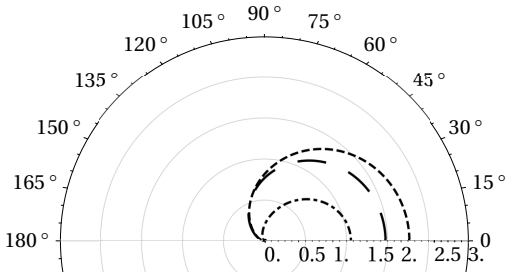

(b) $k_1 = 10$, $k_3 = 1$, Case b).

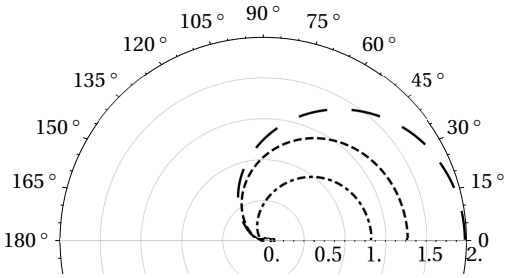

(c) $k_1 = 10$, $k_3 = 5$, Case a).

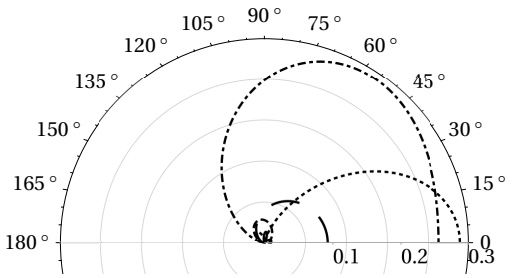

(d) $k_1 = 10$, $k_3 = 5$, Case b).

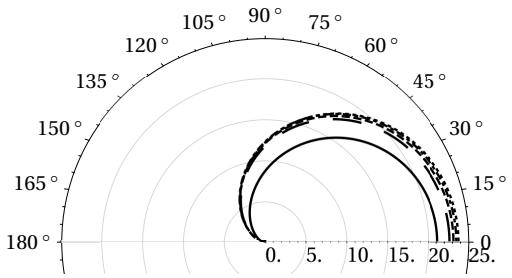

(e) $k_1 = 1$, $k_3 = 1$, Case a).

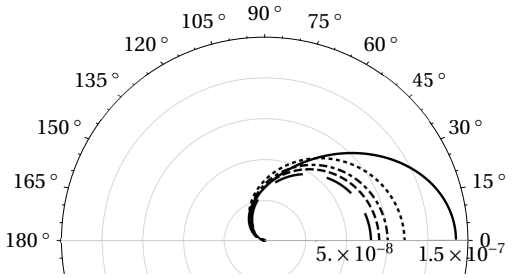

(f) $k_1 = 1$, $k_3 = 1$, Case b).

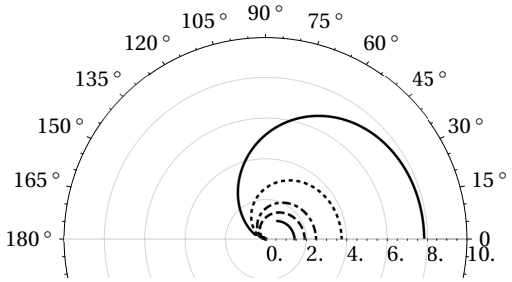

(g) $k_1 = 1$, $k_3 = 5$, Case a).

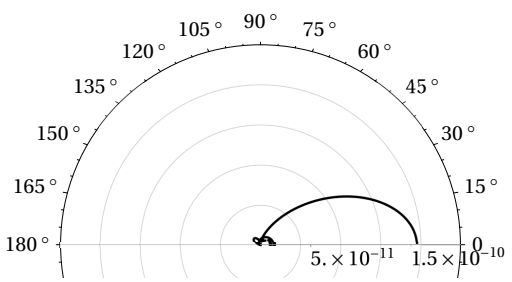

(h) $k_1 = 1$, $k_3 = 5$, Case b).

Figure 7: Polar plot of the spanwise average directivity, $10^3 D_a(r, \theta)$ as given by (4.1), for $r = 10$, $M = 0.3$. Large dashed $c = 0$; dashed $c = 0.5$; dot-dashed $c = 1$; dotted $c = 2$, solid $c = 5$.

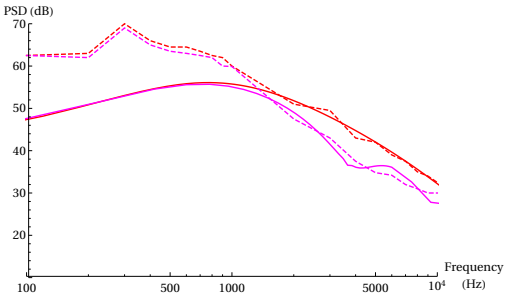

(a) Straight edge $c = 0$ red, and serrated edge $c = 2$ pink.

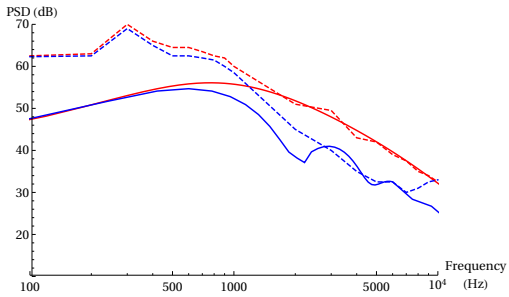

(b) Straight edge $c = 0$ red, and serrated edge $c = 4$ blue.

Figure 8: Comparison of far-field PSD for two serrated leading edges. Solid lines give the analytic results, dashed lines give the experimental measurements.

good agreement at low frequencies due to the dominance of jet noise in the experimental measurements. Similarly at very high frequencies trailing-edge noise dominates the experimental measurements thus we do not expect agreement for frequencies beyond around 10^4 Hz.

We note that whilst the straight-edge analytic PSD is non-oscillatory (as expected for a single scattering location, the leading edge), the serrated PSD results oscillate with increasing frequency. This indicates the destructive interference effect discussed at fixed k_3 values for the individual modes, B_n, remains true for a spectrum of k_3 values.

4.4. *Noise reduction mechanisms*

The mathematical solution allows us to see that the reduction occurs due to two key properties: first the interference between terms in the modal expansion coefficients, $E_n(-w_n \cos\theta)$, which depend on both wavenumber components k_1 and k_3, and the tip-to-root ratio of the serration. Generally destructive interference occur, however constructive interference can also occur at fixed k_3 values and in these cases we see the increase of overall far-field noise. Second; a redistribution energy towards higher modes for large serration heights.

We illustrate these two properties for periodic case b) by considering the modal expansion terms (for simplicity when $k_3 = 0$) given by

$$E_n = \frac{4(-1)^n s \, \sin\left(\frac{s+2n\pi}{4}\right)}{(s+2n\pi)(s-2n\pi)}, \tag{4.4}$$

where $s = \gamma(\kappa + \lambda)$. When evaluating in the far field, we set $\lambda = -w_n \cos\theta$, hence $s = k_1 c\beta^{-2}(1 - M\cos\theta)$. The interference is clearly represented by the oscillatory sine term, which oscillates with varying (reduced) frequency, k_1, and with varying tip-to-root ratio, c.

For small serration heights, $s \to 0$, $E_0 \to 1$ and $E_{n\neq 0} \to 0$ (which is what would be obtained if we did a modal expansion when $F(z) = 0$ for a straight edge). For large s, when $s \gg m$, $E_m \to 0$, but for $s = O(m)$, $E_m \neq 0$, thus the low E_n coefficients tend to zero whilst the higher modes *which do not propagate to the far field* do not tend to zero. Thus there is a redistribution of acoustic energy towards cutoff modes hence the far-field noise decreases.

This simple formula for the modal terms, (4.4), also allows us to predict the rate of noise reduction for increasing tip-to-root ratio. In particular, for large serration heights, $c \gg 1$, $E_n \sim c^{-1}$, therefore the far-field noise reduction in decibels is logarithmic, $\sim \log_{10}(c)$,

which is as predicted via the numerical and experimental investigations of Narayanan *et al.* (2015). This additional noise-reduction mechanism (the redistribution of energy between modes) ensures that even if a constructive interference is occurring in the modal expansion terms, the overall combination of the two mechanisms leads to one observing an overall decrease of noise in the far field (except at low values of c for which the redistribution is less effective).

The modal coefficients arise due to the expansion of the normal velocity on the leading edge. If the leading edge were straight (spanwise infinite), the expansion of a single frequency normal velocity would be into a Fourier series with a single viable mode, $\mathrm{e}^{ik_3\zeta}$, as if we just factored the ζ dependence from the problem. For a serrated edge, the term $\mathrm{e}^{i\kappa\gamma F(\zeta)}$ must be decomposed into the modal basis which is now not a simple Fourier series, but also dependent on $\gamma F(\zeta)$, and requires multiple modes each of which have coefficients dependent on γ and k_3 allowing for individual modes to have a destructive interference and a redistribution of energy among different modes.

4.5. *Numerical results*

In addition to the comparison of the analytic predictions to experimental results (figure 8), here we compare the analytic results, for convective gust plate interaction, to numerical results using an adapted method first presented in Turner & Kim (2017). The original incident field in Turner & Kim (2017) was that of a line vortex which we anticipate to produce different final results. It is however expected that given both incident fields represent upstream turbulence, they will yield qualitatively similar far-field predictions. We shall first use to obtain numerical results in the two cases of a) a walled channel and b) a periodic channel; we shall compare qualitatively with the analytic predictions. This will show a range of different models of turbulence can be used to qualitatively predict the same effects. Different models of incoming turbulence are beneficial as different approaches (e.g. analytical or numerical) are best suited to different incident fields. Second we shall implement a numerical incident gust model in line with the analytical solution to directly compare the results for periodic channels. In the following sections we briefly outline the numerical procedure.

4.5.1. *Description of the numerical solution approach*

The current numerical solutions are achieved by using the same approach published recently by Turner & Kim (2017). The adjustments made for this particular work are to change the leading-edge serration geometry from a sinusoidal to a sawtooth, to implement the periodic condition on the spanwise boundaries, and to alter the incident field. The current computation employs full three-dimensional compressible Euler equations in a conservative form transformed onto a generalised coordinate system:

$$\frac{\partial}{\partial t}\left(\frac{\boldsymbol{Q}}{J}\right)+\frac{\partial}{\partial \xi_i}\left(\frac{\boldsymbol{F}_j}{J}\frac{\partial \xi_i}{\partial x_j}\right)=-\frac{c_0}{L_c}\frac{\boldsymbol{S}}{J}, \tag{4.5}$$

where c_0 is the ambient speed of sound; L_c is a characteristic length scale ($L_c = 10$, i.e. 10 times the serration wavelength in this paper); and, the indices $i = 1, 2, 3$ and $j = 1, 2, 3$ denote the three dimensions. In (4.5), the conservative variable and flux vectors are given by

$$\left.\begin{aligned}\boldsymbol{Q}&=[\rho,\rho u,\rho v,\rho w,\rho e_{\mathrm{t}}]^T,\\ \boldsymbol{F}_j&=[\rho u_j,(\rho u u_j+\delta_{1j}p),(\rho v u_j+\delta_{2j}p),(\rho w u_j+\delta_{3j}p),(\rho e_{\mathrm{t}}+p)u_j]^T,\end{aligned}\right\} \tag{4.6}$$

where $\xi_i = \{\xi, \eta, \zeta\}$ are the generalised coordinates, $x_j = \{x, y, z\}$ are the Cartesian coordinates, δ_{ij} is the Kronecker delta, $u_j = \{u, v, w\}$, $e_{\mathrm{t}} = p/[(\gamma - 1)\rho] + u_j u_j/2$ and

$\gamma = 1.4$ for air. In the current setup, ξ, η and ζ are body fitted coordinates along the grid lines in the streamwise, vertical and lateral directions, respectively. The Jacobian determinant of the coordinate transformation (from Cartesian to the body fitted) is given by $J^{-1} = |\partial(x, y, z)/\partial(\xi, \eta, \zeta)|$ (Kim & Morris 2002). The extra source term $\boldsymbol{S}$ on the right-hand side of (4.5) is arranged to implement a non-reflecting sponge condition which is detailed in Kim *et al.* (2010a,b).

The governing equations given above are solved by using high-order accurate numerical methods specifically developed for aeroacoustic simulations on structured grids as discussed in Turner & Kim (2017). The computational domain is a cuboid that covers $4.5L_c$ (including the sponge layers) in the upstream, vertical and downstream directions from the mean leading edge position. The spanwise length is equal to the serration wavelength. The domain is filled with a structured grid that is uniform in the majority of the domain except in the sponge zone and the local area nearest to the leading edge. A high grid density is maintained in the acoustic field in order to accurately capture the high-frequency components (at least 8 cells per gust wavelength and 10 cells per acoustic wavelength in the upstream direction at the frequency of $k_1 = 10$ in this paper). In total, 22 million grid cells ($768\times448\times64$) are used in the current numerical simulations.

The computation is parallelised via domain decomposition and message passing interface (MPI) approaches. The compact finite difference schemes and filters used are implicit in space due to the inversion of pentadiagonal matrices involved, which requires a precise and efficient technique for the parallelisation in order to avoid numerical artifacts that may appear at the subdomain boundaries. A recent parallelisation approach based on quasi-disjoint matrix systems (Kim 2013) offering super-linear scalability is used in the present paper. The entire domain is decomposed and distributed onto 336 separate processor cores ($12 \times 14 \times 2$ in the streamwise, vertical and spanwise directions, respectively). The parallel computation has successfully been carried out in the IRIDIS-4 computer cluster at the University of Southampton.

4.5.2. *Prescribed spanwise vortex model*

The current numerical simulation employs a spanwise vortex model prescribed as an initial condition, instead of a harmonic vortical gust used for the analytical solution. This approach has an advantage of having a wide range of frequency responses in a single simulation as opposed to running multiple separate simulations each for a single-frequency gust. The vortex model is based on a vector potential function:

$$\boldsymbol{\psi}(\boldsymbol{x}) = \frac{\epsilon}{2\pi} c_0 R \left(\frac{r}{R}\right)^{\frac{3}{2}} \exp\left[1 - \frac{1}{2}\left(\frac{r}{R}\right)^2\right] \boldsymbol{e}_z \quad \text{with} \quad r = \sqrt{(x - x_0)^2 + y^2}, \tag{4.7}$$

where R is a representative length scale of the vortex and $\boldsymbol{e}_z$ is a unit vector in the spanwise direction. The velocity field is created by taking the curl of the vector potential, which provides a divergence-free initial condition:

$$\boldsymbol{u}(\boldsymbol{x}) = \nabla \times \psi(\boldsymbol{x}) = \psi(\boldsymbol{x}) \left\{ M_\infty + \frac{y}{R}\sigma(\boldsymbol{x}) \, , \, -\frac{x - x_0}{R}\sigma(\boldsymbol{x}) \, , 0 \right\}, \tag{4.8}$$

$$\sigma(\boldsymbol{x}) = 1 - \frac{3R^2}{(x - x_0)^2 + y^2}, \tag{4.9}$$

where x_0 is the initial streamwise position of the vortex. The pressure and density are determined by assuming an isentropic flow with its total enthalpy conserved:

$$\rho(\boldsymbol{x}) = \rho_\infty \left[1 - \frac{\gamma - 1}{2}\left(\frac{\psi(\boldsymbol{x})}{c_0 R}\right)^2\right], \quad p(\boldsymbol{x}) = p_\infty \left[\frac{\rho(\boldsymbol{x})}{\rho_\infty}\right]^\gamma. \tag{4.10}$$

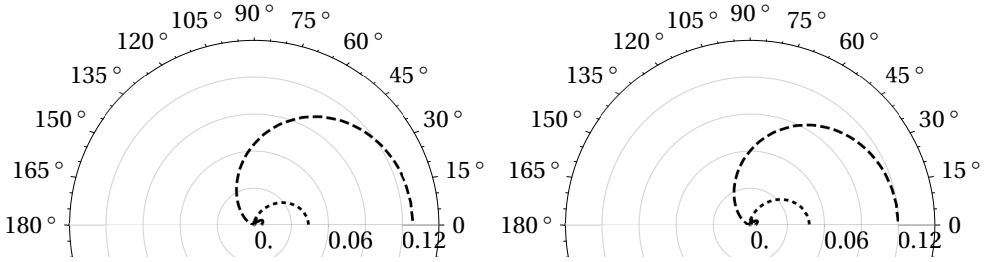

(a) Case a) (b) Case b)

Figure 9: Polar plot of the spanwise average directivity multiplied by frequency, $k_1 D_n(r, \theta)$, found numerically with incident vortex and $r = 10$, $M = 0.3$, $k_3 = 0$, $c = 4$. Dashed $k_1 = 1$; dotted $k_1 = 5$; solid $k_1 = 10$.

The subscript '∞' denotes the free-stream condition. The free-stream Mach number is set to $M_\infty = 0.3$ for the current simulations. The free parameters R and ϵ in (4.7) are set to $R = 0.05L_c$ and $\epsilon = 0.08$, which results in the largest vertical velocity perturbation to reach 5% of the free-stream velocity.

4.5.3. *Prescribed gust model*

A prescribed periodic gust model is also used in the current numerical simulations in order to allow for a direct comparison between the numerical results with the analytic ones in the same scenario. The gust function used in the simulations is identical to (2.2) where $k_2 = k_3 = A_1 = A_3 = 0$ and $A_1 = 0.01c_0$, hence purely vertical velocity perturbations as a function of k_1 (streamwise gust wavenumber). The gust is introduced into the computational domain through the sponge layer – via the source term $\mathbf{S}$ in (4.5) – in the upstream boundary region, of which the details of the implementation are described in Kim *et al.* (2010a,b). Unlike the vortex model introduced above, the gust model contains only one frequency per each simulation case, hence is not suitable to discuss the frequency spectra. It is intended to compare the sound directivity at certain frequencies between the numerical and analytical solutions.

4.5.4. *Comparison of numerical and analytical results*

We first compare the numerical results using the original vortex model from case a) to those from case b) in Figure 9, for fixed serration height with $c = 4$, for varying frequencies, $k_1 = 1, 5, 10$. We define $D_n(r, \theta)$ as the equivalent span-averaged directivity to the analytically defined $D_a(r, \theta)$, and multiply by the frequency to ensure details at $k_1 = 10$ can be viewed. It is clear both case a) and case b) show very similar acoustic directivities in Figure 9 for $k_1 = 1, 5$, which is as predicted analytically by comparing the results in Figures 3 and 6. Through the analytic solution we are able to attribute this to the fact that at these frequencies there is only one scattered mode, and for zero spanwise wavenumber these modes are identical for cases a) and b). For $k_1 = 10$ the directivities differ, also as predicted by the analytic results. Evident too in Figure 9 is the trend of increasing k_1 increasing the modulation of the far-field, which is found analytically.

We next directly compare the numerical and analytical directivity patterns for incident gusts on a logarithmic scale by plotting $10 \log_{10} \left(10^8 D_{n,a}(r, \theta)\right)$ in Figure 10. The value of 10^8 is included to ensure all plotted values are positive and visible. We see good agreement between the results, but some discrepancies at larger frequencies which we attribute to the non-linear effects present in the numerical model; it is known from Turner & Kim (2017) that horseshoe vortices form at the leading edge serration when exposed to an

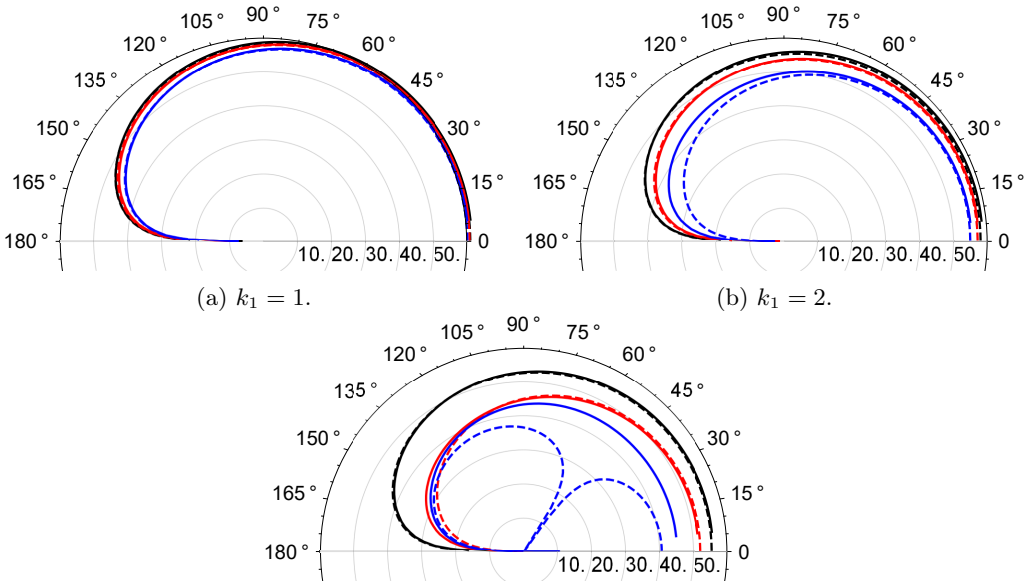

(a) $k_1 = 1$.

(b) $k_1 = 2$.

(c) $k_1 = 4$.

Figure 10: Polar plot of the (scaled) logarithmic spanwise average directivity, $10\log_{10}\left(10^8 D_{n,a}(r,\theta)\right)$ calculated numerically (solid) and analytically (dashed), for different serration height parameters; $c = 0$ (black), $c = 2$ (red), $c = 4$ (blue).

unsteady incident field, and these effects only occur for non-zero serration heights. These horseshoe vortices modify the strength of the acoustic sources at the tip and root of the serration, which in turn causes the tip-and-root interference to be less effective (and therefore numerically there is a disappearance of the perfect cancellations present at certain observer angles in the analytic solution of the far-field pressure). This non-linear effect is not present in the linear analytic model. These non-linear effects become larger for larger values of k_1 and c.

Finally, to compare the two results over a wider range of frequencies, we now consider the far-field sound pressure level (SPL) measured in dB averaged over a cylinder at radius $r = 10$, as a function of reduced frequency k_1. This is defined as

$$\mathrm{SPL} = 10\log_{10}\left(\frac{1}{\pi}\int_0^{\pi}\int_0^1 |p(10,\theta,z)|^2 dz\, d\theta\right). \tag{4.11}$$

We integrate over $\theta \in [0,\pi]$ to capture all oscillatory effects of the far-field directivity which we know are affected by non-linear features in the numerical results. Analytically we restrict to $k_3 = 0$ (and thus do not include a turbulent spectrum). We compare to the numerical line vortex model which has no a spanwise variation in the incident field. We see very good agreement between the analytic and numerical results in Figure 11. The very low frequencies do not agree well as the method of steepest descents required $k_1 r \gg 1$, and this assumption breaks down for small k_1. As expected, the highest c results ($c = 8$) compare least favourably, particularly at high frequencies, again due to the influence of non-linear effects accounted for in the numerical model.

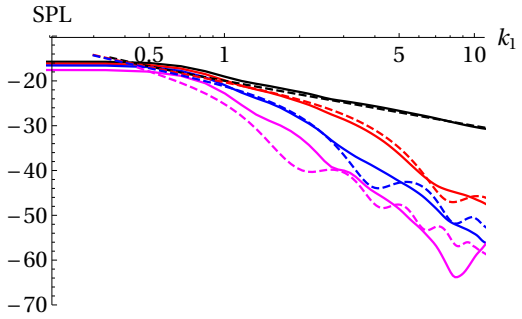

Figure 11: Comparison of the $k_3 = 0$ SPL calculated numerically for a line vortex (solid) and analytically for an incident gust (dashed), for $c = 0$ (black), $c = 2$ (red), $c = 4$ (blue), and $c = 8$ (magenta).

5. Conclusion

This paper has presented an analytic solution for the sound generated by a convective gust interacting with a flat plate with a serrated edge. The plate is in a channel with either rigid walls, or a periodic condition such that the result mimics that of a spanwise semi-infinite blade with leading-edge serration. The solutions follow the method used by Envia (1988) who considered a swept blade in a channel with rigid walls and employed the Wiener-Hopf technique.

The solution both for rigid or periodic walls predicts overall a decrease in far-field acoustic pressure as the height of the serration in increased, however for low frequency incident gusts the reduction of noise is much smaller than at higher frequencies, as is known from experimental, numerical and analytical results (Chaitanya *et al.* 2016; Haeri *et al.* 2015; Lyu & Azarpeyvand 2017). There is little difference between the rigid or periodic cases when the gust has zero spanwise wavenumber, $k_3 = 0$, indicating the key parameters are the gust streamwise wavenumber, k_1, and the greatest distance between points along the leading edge, namely the tip-to-root distance, $c/2$. All of these features are also replicated in numerical results. The numerical method shows good agreement for the far-field SPL verses frequency, k_1, for a range of serration heights, c. This indicates the key noise-reduction mechanisms can be appropriately modelled by the simple analytical solution which uses an incident gust.

The analytical solution relies on a modal decomposition of the incident and scattered fields, however this is not simply a Fourier series expansion, but a modal expansion which depends intrinsically on the leading-edge geometry. Because of this choice of modal basis, the expansion coefficients can be calculated analytically thus the acoustic pressure can be computed for any parameters incredibly quickly; span-averaged directivities can be plotted in approximately 6 seconds on a standard 4-core desktop computer (via Mathematica). The modal coefficients also shed light on the mechanisms behind the noise reduction as we see they lead to two key features. First, the coefficients are oscillatory indicating interference in the acoustic pressure in the far field. This interference commonly is destructive and reduces the scattered noise, but in some cases of non-zero k_3 has been seen to increase the scattered noise (i.e. is constructive). Second, as the tip-to-root distance of the serration, $c/2$, increases, the expansion coefficients vary, with lower modes tending to zero. Higher modes do not tend to zero but are cutoff. Thus increasing the tip-to-root distance redistributes acoustic energy from the lower (cuton) modes to higher (cutoff) modes hence significant far-field noise reductions can be achieved for large tip-to-root distances. This second noise reduction mechanism means that even if a

constructive interference were to occur, an overall noise reduction would be observed in the far-field.

The rate at which the cuton modes decrease with increasing serration height is proportional to $1/c$, thus it is predicted as c increases the reduction of noise in decibels is logarithmic, $\sim \log_{10}(c)$, as alluded to in Narayanan *et al.* (2015). A logarithmic noise reduction dependency indicates that continuing to increase the tip-to-root serration height lessens the level of noise reduction. Therefore, since increasing the tip-to-root height decreases aerodynamic performance, for a given application of serrated leading edges, it is likely an optimum serration height yielding a significant noise reduction could be determined for a prescribed limited decrease of aerodynamic performance. However obtaining further noise reductions, whilst possible by further increasing the tip-to-root height, would be too costly on aerodynamic performance. Other leading-edge designs, such as the hook structures from (Chaitanya *et al.* 2016) (comprised of a sawtooth serration with an additional v-shaped cut in the root), could allow the same tip-to-root ratio as a simple serration, but greater aerodynamic efficiency due to a greater leading-edge surface area. Therefore much work is still needed to consider more complicated leading-edge geometries and the potential for optimal noise reduction with minimal aerodynamic impact.

Acknowledgements

The authors would like to acknowledge the support from EPSRC Fellowship EP/P015980/1 (L.A.). Also, the authors would like to thank EPSRC for the computational time made available on the UK supercomputing facility ARCHER via the UK Turbulence Consortium (EP/R029326/1), and IRIDIS-4 at the University of Southampton (J.W.K.) for the completion of the work.

Appendix A. Expansion Coefficients, $E_n(\lambda)$

The expansion coefficients are obtained by

$$E_n = \epsilon_n^{-1} \int_0^1 \mathrm{e}^{i\kappa\gamma F(\zeta)+ik_3\zeta} \overline{Z_n(\bar{\lambda},\zeta)} d\zeta, \tag{A.1}$$

where the overbar denotes the complex conjugate, and ϵ_n are normalisation coefficients

$$\epsilon_n = \int_0^1 Z_n(\lambda,\zeta)\overline{Z_n(\bar{\lambda},\zeta)} d\zeta. \tag{A.2}$$

When Z_n is given by (3.7) (case a),

$$E_0 = \frac{2\mathrm{e}^{ik_3/2}}{(k_3-s)(k_3+s)} \left((k_3-s)\sin\left[\frac{k_3}{2}\right] + 2s\,\sin\left[\frac{1}{4}(k_3-s)\right]\right), \tag{A.3}$$

$$\begin{aligned} E_n =& \frac{\mathrm{e}^{-\frac{is}{4}}}{((k_3+s)^2-n^2\pi^2)((k_3-s)^2-n^2\pi^2)} \left[2\mathrm{e}^{\frac{is}{4}}\left(1-(-1)^n\mathrm{e}^{ik_3}\right)(k_3+s)((k_3-s)^2-n^2\pi^2)\right. \\ &+ 4is(k_3^2-s^2+n^2\pi^2)\cos\left[\frac{n\pi}{4}\right]\left(\mathrm{e}^{\frac{i}{4}(k_3+2s)}-(-1)^n\mathrm{e}^{\frac{3ik_3}{4}}\right) \\ &\left.+8k_3n\pi s\sin\left[\frac{n\pi}{4}\right]\left(\mathrm{e}^{\frac{i}{4}(k_3+2s)}+(-1)^n\mathrm{e}^{\frac{3ik_3}{4}}\right)\right], \end{aligned} \tag{A.4}$$

where $s=\gamma(\kappa+\lambda)$.

When Z_n is given by (3.8) (case b),

$$E_0 = \frac{2\mathrm{e}^{iq/2}}{s^2-q^2}\left(2s\sin\left[\frac{s-q}{4}\right] + (s-q)\sin\left[\frac{q}{2}\right]\right), \tag{A.5}$$

$$E_n = \frac{-i\mathrm{e}^{-is/4}}{(s+2n\pi-q)\,(s-2n\pi+q)}\left(2i^n s\mathrm{e}^{3iq/4}\left(-1+\mathrm{e}^{i(s+2n\pi-q)/2}\right) + \mathrm{e}^{is/4}(e^{iq}-1)(s+2n\pi-q)\right), \tag{A.6}$$

where $q = k_3(1+\alpha)$. We note that all singularities in these E_n are removable, thus there are no poles.

REFERENCES

Adamczyk, J. J. 1974 Passage of a swept airfoil through an oblique gust. *Journal of Sound Aircraft* **11**, 281–287.

Amiet, R. K. 1975 Acoustic radiation from an airfoil in a turbulent stream. *Journal of Sound and Vibration* **41**, 407–420.

Ayton, L. J. & Chaitanya, P. 2017 Analytical and experimental investigation into the effects of leading-edge radius on gust-aerofoil interaction noise. *Journal of Fluid Mechanics* , .

Chaitanya, P., Narayanan, S., Joseph, P. F. & Kim, J. W. 2016 Leading edge serration geometries for significantly enhanced leading edge noise reductions. *22nd AIAA/CEAS Aeroacoustics* AIAA 2016-2736.

Envia, E. 1988 *Influence of Vane Sweep on Rotor-Stator Interaction Noise.*. PhD thesis, University of Arizona.

Geyer, T. F., Wasala, S. H., Cater, J. E., Norris, S. E. & Sarradj, E. 2016 Experimental Investigation of Leading Edge Hook Structures for Wind Turbine Noise Reduction. *22nd AIAA/CEAS Aeroacoustics* AIAA 2016-2954.

Goldstein, M. E. & Atassi, H. 1976 A complete second-order theory for the unsteady flow about an airfoil due to a periodic gust. *Journal of Fluid Mechanics* **74**, 741–765.

Graham, R. R. 1934 The silent flight of owls. *Journal of the Royal Aeronautical Society* **38**, 837–843.

Haeri, S., Kim, J. W. & Joseph, P. 2015 On the mechanisms of noise reduction in aerofoil-turbulence interaction by using wavy leading edges. *21st AIAA/CEAS Aeroacoustics Conference, Dallas, TX*, AIAA 2015-3269.

Huang, X. 2017 Theoretical model of acoustic scattering from a flat plate with serrations. *Journal of Fluid Mechanics* **819**, 228–257.

Kim, J. W. & Morris, P. J. 2002 Computation of subsonic inviscid flow past a cone using high-order schemes. *AIAA Journal* **40**, 1961–1968.

Kim, J. W., Lau, A. S. H. & Sandham, N. D. 2010 Boundary conditions for airfoil noise due to high-frequency gusts. *Periodica Engineering* **6**, 244–253.

Kim, J. W., Lau, A. S. H. & Sandham, N. D. 2010 Proposed boundary conditions for gust-airfoil interaction noise. *AIAA Journal* **48**, 2705–2709.

Kim, J. W. 2013 Quasi-disjoint pentadiagonal matrix systems for the parallelization of compact finite-difference schemes and filters. *Journal of Computational Physics* **241**, 168–194.

Kim, J. W., Haeri, S. & Joseph, P. F. 2016 On the reduction of aerofoil–turbulence interaction noise associated with wavy leading edges. *Journal of Fluid Mechanics* **792**, 526–552.

Lilley G. M. 1998 A study of the silent flight of the owl. *4th AIAA/CEAS Aeroacoustics Conference, Toulouse*, AIAA 1998-2340.

Lockard, D. P. & Morris, P. J. 1998 Radiated noise from airfoils in realistic mean flows. *AIAA Journal* **36**, 907–914.

Lyu, B., & Azarpeyvand, M. 2017 On the noise prediction for serrated leading edges . *Journal of Fluid Mechanics* **826**, 205–234.

Mathews, J. & Peake, N. 2018 An analytically-based method for predicting the noise generated by the interaction between turbulence and a serrated leading edge. *Journal of Sound and Vibration* **422**, 506–525.

Myers, M. R. & Kerschen, E. J. 1995 Influence of incidence angle on sound generation by airfoils interacting with high-frequency gusts. *Journal of Fluid Mechanics* **292**, 271–304.

Narayanan, S., Chaitanya, P., Haeri, S., Joseph, P. F., Kim, J. W. & Polacsek, C. 2015 Airfoil noise reductions through leading edge serrations. *Physics of Fluids* **27**.

Peake, N. & Parry, A. B. 2012 Modern challenges facing turbomachinery aeroacoustics. *Annual Review of Fluid Mechanics* **44**, 227–248.

Turner, J. M. & Kim, J. W. 2017 Aeroacoustic source mechanisms of a wavy leading edge undergoing vortical disturbances. *Journal of Fluid Mechanics* **811**, 582–611.